Pilot-Scale Continuous Synthesis of a Vanadium-Doped $LiFePO_4$/C Nanocomposite High-Rate Cathode for Lithium-Ion Batteries

Ian D. Johnson,[1] Mechthild Lubke,[1] On Y. Wu,[1] Neel M. Makwana,[1] Glen J. Smales,[2] Husn U. Islam,[1] Rashmi Y. Dedigama,[1] Robert I. Gruar,[1] Christopher J. Tighe,[1] David O. Scanlon,[2] Furio Corà,[1] Dan J. L. Brett,[3] Paul R. Shearing,[3] and Jawwad A. Darr[1*]

*Corresponding author: Professor Jawwad A. Darr
Christopher Ingold Laboratories, Department of Chemistry, University College London
20 Gordon Street, London, WC1H 0AJ
j.a.darr@ucl.ac.uk
Office telephone: +44 (0)20 7679 4345
Fax: +44 (0)20 7679 7463
Mobile: +44 (0)7941 928875
Research webpages http://www.ucl.me.uk

Abstract

A high performance vanadium-doped $LiFePO_4$ (LFP) electrode is synthesized using a continuous hydrothermal method at a rate of 6 kg per day. The supercritical water solvent rapidly generates core/shell nanoparticles with a thin, continuous carbon coating on the surface of LFP, which aids electron transport dynamics across the particle surface. Vanadium dopant concentration has a profound effect on the performance of LFP, where the composition $LiFe_{0.95}V_{0.05}PO_4$ achieves a specific discharge capacity which is among the highest in the literature (119 mA h g^{-1} at a discharge rate of 1500 mA g^{-1}). Additionally, a combination of X-ray absorption spectroscopy analysis and hybrid-exchange density functional theory suggest that vanadium ions replace both phosphorous and iron in the structure, thereby facilitating Li^+ diffusion due to Li^+ vacancy generation and changes in the crystal structure.

Keywords: lithium-ion battery, phosphate, doped, continuous hydrothermal synthesis, high power, cathode

For submission to J. Power Sources

Pilot-Scale Continuous Synthesis of a Vanadium-Doped $LiFePO_4$/C Nanocomposite High-Rate Cathode for Lithium-Ion Batteries

Ian D. Johnson,[1] Mechthild Lubke,[1] On Y. Wu,[1] Neel M. Makwana,[1] Glen J. Smales,[2] Husn U. Islam,[1] Rashmi Y. Dedigama,[1] Robert I. Gruar,[1] Christopher J. Tighe,[1] David O. Scanlon,[2] Furio Corà,[1] Dan J. L. Brett,[3] Paul R. Shearing,[3] and Jawwad A. Darr[1*]

[1] Department of Chemistry, University College London, 20 Gordon Street, London, WC1H 0AJ, U.K.

[2] Diamond Light Source Ltd, Diamond House, Harwell Science and Innovation Campus, Didcot, Oxfordshire, OX11 0DE, U.K.

[3] Department of Chemical Engineering, University College London, Torrington Place, London, WC1E 7JE, U.K

1. Introduction

Olivine lithium iron phosphate (LFP) and its doped analogues have received significant attention for use as cathode materials in Li-ion batteries since their discovery by Goodenough *et al* [1]. The properties of $LiFePO_4$ make it a promising candidate to replace $LiCoO_2$ and other lithium transition metal oxides in many commercial secondary batteries. $LiFePO_4$ offers, in theory, a moderate capacity of 170 mA h g^{-1}, relatively high thermal stability compared to $LiCoO_2$ and contains abundant, inexpensive and non-toxic elements [2]. Unfortunately, pure bulk $LiFePO_4$ possesses low electronic conductivity and ionic diffusivity, reported to be in the range of 10^{-9} to 10^{-8} S cm^{-1} and 10^{-17} to 10^{-12} cm^2 s^{-1} respectively [3-5], which results in low discharge capacity at high discharge rates. To some degree, these limitations have been addressed by reducing the crystallite size and incorporating dopants such as Nb, V, and Mg to modify the crystal structure and improve bulk electronic conductivity [6-8]. In addition, the use of conducting carbons or polymer coatings on the particle surface has increased conductivity and discharge capacity [9,10].

Vanadium-doped $LiFePO_4$ is of particular interest as a high-rate cathode material in Li-ion batteries, as doping has been found to increase discharge capacity at high discharge rates. The literature, however, contains conflicting findings with respect to the synthesis, phase behavior and performance of these materials. Some researchers have found the best performance is observed when vanadium is found exclusively within the olivine structure [11]. This has been attributed to decreased Li^+ diffusion activation energy barriers and increased electrical conductivity within the material [12]. Structural refinement has indicated the V ions can either occupy Fe or Li sites within LFP depending upon the stoichiometry of the precursors [13-17]. Vanadium has also been found to occupy the P site [8], although later attempts to repeat this substitution were unsuccessful [15]. However, optimal performance has also been found if vanadium-containing impurities such as $Li_3V_2(PO_4)_3$ or VO_2 are present at the surface of the particles [15,18,19]. These are thought to improve electron and Li^+ transport dynamics between the particle surface and the surrounding cathode carbon matrix and electrolyte. These conclusions are supported by atomistic modelling research, which suggested aliovalent doping is impossible in $LiFePO_4$ on energetic grounds [20]. Therefore there is still some debate regarding the exact nature of V-doping in these materials, and how they benefit the electrochemical performance.

The synthesis of carbon-coated $LiFePO_4$ (hereafter referred to as $LiFePO_4$/C) has been achieved through a number of methods, including solid-state and hydrothermal syntheses [21-23]. Solid-state reactions currently account for most industrial-scale syntheses of $LiFePO_4$/C, although there is increasing interest in alternative methods as the solid-state synthesis process usually involves high temperatures, multiple steps and lengthy heat-treatments. In contrast, batch hydrothermal reactions typically require lower synthesis temperatures. By incorporating surfactants, some degree of control over particle size and morphology can be achieved, although inevitably the use of surfactants adds additional cost and complexity [24,25].

Continuous synthesis in flow processes is considered advantageous over batch type synthesis routes, as the former processes are often more flexible and can allow independent control over more reaction variables, and can rapidly convert ions in solution to the solid, often generating kinetic products. In continuous hydrothermal synthesis, a flow of supercritical water is mixed with aqueous metal salt in a well-defined mixer arrangement, resulting in rapid reaction of the aqueous metal salt to form nanoparticles. Continuous hydrothermal reactors have already been used for the production of nanoparticle metal oxides, and more recently have been extended to phosphates [26-29]. Continuous hydrothermal synthesis of $LiFePO_4$ was reported by Xu *et al.*, where a precursor ratio of 1:1:3 $FeSO_4$:H_3PO_4:LiOH produced phase-pure $LiFePO_4$ for both subcritical and supercritical water feeds [30]. The use of supercritical water gave an increase in particle size compared to the subcritical case (made at a scale of *ca*. 0.3 g h^{-1} assuming 100% yield). In contrast, Hong *et al.* found crystallite sizes were smaller when supercritical water was used as a feed (100 nm, with numerous morphologies) as opposed to subcritical water (> 1 µm, with rhombic morphology), although in both cases there was significant variation in size and morphology with conditions (made at a scale of *ca*. 0.5 g h^{-1} assuming 100% yield) [31]. A residence time of around 40 s was required to give the pure olivine phase. In contrast, Aimable *et al*. were able to synthesize $LiFePO_4$ with a residence time of 12 s by using a Fe:P:Li ratio of 1:1:3.75 [32]. However, of the materials that were tested, the best high-rate performance of $LiFePO_4$ yielded a comparatively modest capacity (105 mA h g^{-1} at 1 C). To our knowledge, there are no reports of scaled-up continuous synthesis of doped $LiFePO_4$ or $LiFePO_4$/C nanomaterial in the academic literature which provide high capacity and high-rate performance, although we are aware of commercial research in industry from Hanwha Corporation in Korea [33].

The purpose of this study is to generate a high performance LFP-based electrode using a continuous, low-temperature hydrothermal process. We attempted to generate nanoparticulate

LFP with a uniform carbon coating by including a carbon source (fructose) in the precursors, and further improve the rate capability by incorporating varying levels of vanadium dopant in the structure. We utilize a combination of experimental and theoretical techniques to indicate the location and effect of vanadium, and aim to provide a new insight into the behavior of these doped materials.

2. Experimental section

2.1. Synthesis

Carbon-coated vanadium-doped lithium iron phosphate samples (where the C is amorphous) was synthesized using a pilot-scale continuous hydrothermal flow synthesis (CHFS) reactor incorporating a confined jet mixer (CJM), the design of which has previously been described in detail [34], and schematics of both are shown in **Figure S1** and **Figure S2** respectively. Briefly, two aqueous solutions were prepared from the following precursors. The first solution consisted of $FeSO_4 \cdot 7H_2O$ (99+%, Alfa Aesar, Heysham, UK), $VOSO_4 \cdot 5H_2O$ (17-23% V, Acros Organics, Loughborough, UK), 0.375 M H_3PO_4 (85-88% wt%, Sigma Aldrich, Steinheim, Germany) and fructose (99%, Alfa Aesar, Heysham, UK) in deionized (D.I.) water. The composition of the first solution was varied in separate experiments as described in **Table S1**, where the sum of [Fe] and [V] was 0.25 M and the concentration of fructose was 0.65 – 0.75 M. The second solution contained 0.8625 M $LiOH \cdot H_2O$ (99+%, Fischer Scientific, Loughborough, UK) in D.I. water. Each solution was pumped into a T-piece mixer (0.25" internal diameter) with a flow rate of 200 mL min^{-1} each. The combined mixture of solutions 1 and 2 flowed at 400 mL min^{-1} into the side arms of the CJM, where it rapidly combined with 400 mL min^{-1} (referred to 0.1 MPa and 20 ^{o}C) of supercritical water at 450 °C and 24.1 MPa which emerged from the inner tube of the CJM as a turbulent jet (**Figure S2**), resulting in extremely rapid mixing [34]. The nanoparticles of $LiFePO_4$/C (either pure of doped with V) rapidly formed in the mixture at a temperature of *ca.* 335 °C [35]. The mixture

was held at this temperature as it flowed through the outlet pipe with a residence time of *ca.* 6.5 s before cooling to near ambient temperature through a pipe-in-pipe countercurrent heat exchanger. The cooled slurry passed through a back-pressure regulator (BPR, Swagelok KHB series) which maintained the system pressure at 24.1 MPa, after which it was collected in a plastic container open to the atmosphere. The slurry was allowed to settle out and the supernatant (containing unreacted precursors and by-products) siphoned off. The concentrated slurry was further concentrated using a centrifuge (4500 r.p.m, 10 minutes), and mixed with 500 g D.I. water (resistivity > 10 MΩ) with shaking and centrifuged (4500 r.p.m, 10 minutes). This process of centrifuging and washing was repeated before the cleaned, wet product was placed in a freeze-drier (Virtis Genesis 35XL) and slowly heated from -60 °C to 25 °C, over 24 h under vacuum of < 100 mTorr. The freeze-dried powder was subsequently heat-treated from ambient temperature up to 700 °C and held for 3 hours, with a heating rate of 5 °C min^{-1} under a flow of argon.

2.2. Characterization

XRD patterns were obtained on a Bruker D4 Endeavour diffractometer using Cu-Kα radiation (λ = 1.54 Å) over the 2θ range 5 - 60° with a step size of 0.05° and a count time of 2 s or 4 s. The diffractometer was configured in the Bragg-Brentano flat-plate reflection geometry, with a post-sample graphite monochromator selecting both $K_{\alpha 1}$ and $K_{\alpha 2}$. A scintillation counter detector was used with 0.5° divergent and receiving slits. High-quality XRD patterns of the samples were obtained on a STOE StadiP diffractometer in a 0.3 mm borosilicate glass capillary using Mo-Kα radiation (λ = 0.71 Å) over the 2θ range 5 - 60° with a step size of 0.5° and step time of 87 s. The diffractometer was configured in the Debye-Scherrer geometry with a Dectris Mython 1k silicon strip detector covering 18° 2θ. LeBail analysis was performed using MAUD (Material Analysis Using Diffraction) software [36].

Raman spectra were collected on a Raman microscope system (Renishaw inVia^{TM}) with a laser excitation wavelength of 514.5 nm; the laser power was set to 10 % of full power for all samples. Scans were conducted over the range 200-2000 cm^{-1}; each individual scan lasted 30 s, and the sum of 4 individual scans produced the spectra, giving a total scan time of 2 minutes. The size and morphology of the heat-treated particles and the distribution of Fe and V within them were determined by TEM and EDS (Jeol JEM-1010 fitted with an Oxford Instruments X-MaxN 80-T Silicon Drift Detector (SDD)) and processed using AZtec® software. Field emission scanning electron microscopy (FE-SEM) images were obtained using a JEOL JSM-6700F microscope.

Chemical analysis for Li, Fe, V and P was performed by ICP-AES using dilute solutions of the samples dissolved in 1% HNO_3 (aq.) (Department of Earth Sciences, University College London).

Transmission measurements were taken of the sample at the vanadium K-edge (*ca.* 5465 eV) at B18, Diamond Light Source using ion chambers to measure incident and transmitted beams. XAS data reduction and EXAFS modelling were performed on Horae Athena and Excurve 9.273 respectively [37,38].

2.3. Electrode preparation and electrochemical characterization

The cathode was prepared by mixing 80 wt% heat-treated sample, 10 wt% conductive agent (carbon black, Super P^{TM}, Alfa Aesar UK) and 10 wt% Polyvinylidene fluoride, PVDF (PI-KEM, Staffordshire, UK). The PVDF was dispersed in N-Methyl-2-pyrrolidone, NMP (Sigma Aldrich, St. Louis, USA) for at least 1 hour at room temperature to ensure it was fully dissolved before adding the other two components. The mixture was ball-milled for 1 h, and the resultant slurry was cast on aluminum foil (PI-KEM, Staffordshire, UK) which was dried in an oven. Circular electrodes (with diameter of 16 mm) were punched out and pressed with a pressure of 1.5 tons cm^{-2}. The electrodes therefore had active material: carbon: binder ratios

shown in **Table S1**. These slurries possessed active mass percentages of 72.6 wt% for ΔLFP1, 69.8 wt% for ΔLFP2 and 76.9-77.5 wt% for the V-doped samples ΔLFVP(2.5) - ΔLFVP(20), corresponding to carbon contents of 17.4 wt%, 20.2 wt% and 12.5-13.1 wt% respectively. The capacity of the electrodes was calculated based on the proportion of active material in the electrode and the measured mass of the electrode. The active mass loadings for all electrodes tested were in the range 1.9-2.3 mg cm^{-2} and had a thickness of approximately 40 µm (measured by FE-SEM), apart from electrodes used for the calculation of the diffusion coefficient, which were approximately 3 mg cm^{-2}.

Electrochemical experiments were performed on two electrode 2032-type coin cells, which were assembled in an argon-filled glovebox (MBraun UNIlab, Nottinghamshire, UK) with O_2 and H_2O maintained below 10 ppm. The counter electrode was lithium metal foil (PI-KEM, Staffordshire, UK). The separator, a glass microfiber filter (WHATMAN, Buckinghamshire, UK), was saturated with an organic electrolyte ($LiPF_6$ in 3:7 wt% ethylene carbonate/ethyl methyl carbonate, LP57 electrolyte from BASF, Ludwigshafen, Germany).

Electrochemical measurements were performed using an Arbin Instruments (CALTEST Instrument Ltd, Guildford, UK) at room temperature of 20 °C. The electrochemical performance was investigated by cyclic voltammetry in the range 2 to 4 V and 2 to 4.3 V vs Li/Li^+ with scan rates between 0.05 and 2 mV s^{-1}. Galvanostatic charge/discharge cycling tests (specific current tests) were performed in the range of 2 to 4 V vs. Li/Li^+, applying variable specific currents between 50 and 1500 mA g^{-1} during charge and discharge. The specific current tests were performed at 50, 100, 150, 200, 500, 750, 1000 and 1500 mA g^{-1}. The specific current and specific capacity was calculated based on the mass of active material (i.e. pure or V-doped $LiFePO_4$) in each printed electrode.

3. Results and Discussion

Pure and V-doped $LiFePO_4$/C were successfully synthesized in the pilot-plant continuous hydrothermal flow synthesis (CHFS) process [34]. Samples named LFP1 and LFP2 are both pure $LiFePO_4$ samples coated with amorphous carbon, and samples named LFVP(x) [x = 2.5, 5, 10, and 20] are similarly carbon-coated vanadium-doped $LiFePO_4$ samples, where x is the nominal vanadium at% (relative to total transition metal content). These samples were all heat-treated (to graphitize the carbon coatings) to give the corresponding samples named ΔLFP1, ΔLFP2 and ΔLFVP(x). The as-prepared samples after freeze-drying were generally fine, grey-blue powders, and heat-treatment of these samples gave black powders, where the graphitization of the carbon layer was confirmed by Raman spectroscopy (**Figure S3**).

3.1. Determination of Structure

X-Ray Diffraction (XRD) patterns of the as-prepared and heat-treated samples all showed the pure olivine structure (**Figure 1a**) was present which had a good match to JCPDS reference pattern number 00-040-1499. However, the samples ΔLFVP(10) and ΔLFVP(20) showed evidence of phase-separation to give a minor $LiV(P_2O_7)$ phase (good match to JCPDS reference pattern 00-085-2381, **Figure 1b**). Significant peak broadening was observed in the as-prepared olivine structures as the vanadium levels increased, which may be indicative of increasing lattice strain. The ability to achieve such a high dopant concentration (*ca*. 20 at%) in the as-prepared material was confirmed by inductively coupled plasma atomic emission spectroscopy (ICP-AES) (**Table 3**). The author thus suggests that this phase was a low temperature metastable product, which was only accessible due to the relatively low synthesis temperature (335 ^{o}C) and rapid conversion from precursor to product in the process, which occurs on a timescale of seconds or less. These dopant levels were in an excess of those normally found in the thermodynamic products, which are often made by higher synthesis temperature techniques [16]. The ability of CHFS-made materials to display increased dopant concentration in a host structure (compared to that achieved before) has previously been

reported for other systems such as the extension of fluorite phase fields within the Ce-Zr-Y-O and Ce-Zn-O nanoparticle phase diagram [39-41].

LeBail fits of high-resolution XRD patterns were used to determine changes in lattice parameter with increasing vanadium content (**Table 1** and **Figure S4-8**). While the *a* lattice parameter and the unit cell volume *V* are virtually invariant with increasing vanadium dopant, the *b* and *c* parameters generally decreased and increased respectively. There is therefore significant distortion of the unit cell with only minor deviation of the volume, and could indicate a more complex doping mechanism than vanadium substitution on a single site. The effect on the *b* and *c* parameters has been commonly observed in other reports of V-doped $LiFePO_4$, and these changes in the unit cell were found to lengthen the Li-O bond lengths and increase the ionic diffusion of Li^+ [8,15,16]. This suggests that the observed changes in the crystal structure were likely to be in part responsible for the improved performance of the doped samples.

Transmission Electron Microscopy (TEM) images of the heat-treated samples all showed significant agglomeration of the nano-sized crystallites to form fused networks (**Figure 2**). The continuous, core/shell nature of the carbon coating was evident, and the carbon loading (quantified by CHN analysis) was consistent between the V-doped samples (range of 3.1-3.8 wt%, **Table S1**). Sample ΔLFP2 had spherical crystallite morphology, with <100 nm crystallite diameter. Upon increasing V content, the crystallite morphology and size changed markedly, with a larger platelet morphology (>100 nm plate diameter) becoming more pronounced at higher doping levels although there was significant variation in particle size and shape within samples. The contrasting morphology between samples ΔLFP2 and ΔLFVP(20) was additionally confirmed by FE-SEM microscopy (**Figure S9**). Further investigation of the effect of vanadium doping on the surface energies and equilibrium

particle morphologies of LFP using computational techniques could provide a deeper understanding for the changes of morphology observed.

Energy-dispersive X-ray spectroscopy (EDS) analysis of sample ΔLFVP(5) indicated a uniform dispersion of metals within the particles, implying homogenous doping of vanadium (**Figure 3a-c**). Therefore, the increased performance of this sample cannot be attributed to the presence of impurities, and must be an effect of vanadium incorporated within the olivine structure. However, the sample with 10 at% vanadium content showed evidence of the phase-separation observed in the powder XRD analysis, with nucleation of a V-rich phase on the surface of the particles (**Figure 3d-g**). Elemental analysis of the impurity phase *via* EDS gave an approximate V:P ratio of 1:2, which is consistent with $LiV(P_2O_7)$, and the presence of this phase may additionally affect cathode performance.

Vanadium K-edge extended X-Ray absorption spectroscopy (EXAFS) data were collected and analyzed for ΔLFVP(2.5) to provide insight into the local structure of the metal ions. The first shell analysis of ΔLFVP(2.5) revealed a mixture of V-O bond lengths present in the material; 49 ± 5 % V-O bonds of length 1.68 ± 0.012 Å, and 50 ± 8 % V-O bond lengths at 2.01 ± 0.016 Å (**Figure 4** and **Table S2**). To facilitate the assignment of these EXAFS observations, a systematic computational DFT study of V-doped LFP was performed under periodic boundary conditions. The method and computational details are identical to those used to study pure LFP, Fe- and V-doped aluminophosphates (AlPOs) [42-44]. The stability of multiple oxidation states of vanadium and the flexibility of the olivine structure enable several modes of incorporation of V ions into LFP: with oxidation states of 2+, 3+, 4+ and 5+ in the Fe site, 4+ and 5+ in the P sites, and 2+ and 3+ in the Li sites. Full geometry optimizations were attempted for these configurations, and the effect of concentration was examined using supercells of different sizes (between 4 and 16 LFP formula units).

Isovalent defects (V^{2+}/Fe^{2+} in $LiFePO_4$, V^{3+}/Fe^{3+} in $FePO_4$, V^{5+}/P^{5+} in $FePO_4$ and $LiFePO_4$) required no additional defect. Aliovalent replacements were charge-balanced by these additional defects: V^{4+} and V^{5+} in the Fe site by Li^{+}/Fe^{3+} or by combined Li and Fe vacancies; V in the Li sites by Fe vacancies and V^{4+}/P^{5+} in $LiFePO_4$ by oxidizing one Fe^{2+} ion to Fe^{3+}.

A summary of equilibrium V-O bond distances for all configurations that converged is reported in **Table 2**. Some of the vanadium oxidation states were unstable to internal redox transformations; V^{4+} in the P^{5+} site with a Fe^{3+} defect in $LiFePO_4$ reverts to V^{5+} and Fe^{2+} and V^{5+} in an Fe^{3+} site reduced spontaneously to V^{4+} by oxidizing an oxide (O^{2-}) ion to an O^{1-} radical next to the charge-balancing defect (Li^{+}/Fe^{3+} or Fe vacancy). The presence of O^{-} is not surprising, and can be explained by the destabilization of the O-2p energy levels next to the low valent cation (Li^{+}/Fe^{3+} or Fe vacancy in this case) which are raised above the V^{5+} 3d acceptor levels. A similar result occurs for all oxidation states of V in Li sites, thereby discounting the location of V in Li sites in the material. This electronic instability is not intrinsic to V^{5+}/Fe^{3+} or V in Li sites, but is rather associated with the charge-balancing defects induced by the hypervalent replacement, and agrees with earlier observations that supervalent dopant incorporation is unstable [45]. For each oxidation state and coordination number of V, we note in **Table 2** that the calculated V-O bond distances (both individually and as average) are little affected by composition and counter-defects; they are therefore a local signature of the V electronic state and coordination environment. Hence measured V-O bond distances are diagnostic of the oxidation state and mode of incorporation of V in LFP.

Among the local environments of V described in **Table 2**, only two offer a close match to the V-O bond distances measured experimentally by EXAFS; these are V^{3+}/Fe^{3+} and V^{5+}/P^{5+}. The assignment of the short 1.68 Å V-O bonds, in particular, can only be attributed to tetrahedral V^{5+}, whose presence in LFP has traditionally been discounted [20]. The

combination of EXAFS measurements and high-level quantum chemical calculations show instead that both octahedral V^{3+} in Fe sites and tetrahedral V^{5+} in P sites are present in this sample, with an approximate ratio of 40:60. The effect of vanadium incorporation is clearly reflected in the lattice parameters found by XRD, and implied the substitution of V on these sites increases the Li^{+} diffusion coefficient due to changes in the unit cell structure.

The V-doped LFP samples made herein *via* CHFS have been obtained starting from a V^{4+} salt ($VOSO_4$) in a reducing environment resulting from the partial breakdown of fructose (the carbon source) under the extreme hydrothermal conditions. Vanadyl salts alone in similar synthetic conditions can reduce to V^{3+} (V_2O_3) [46]. Therefore, the presence of V^{5+} in the samples is counterintuitive and needs understanding. To investigate the possible origin of V^{5+} we performed a new set of calculations, incorporating equal amounts of V^{4+} ions in both Fe and P sites giving charge-neutral phases. Such dual mode of incorporation is typical of 4+ dopant ions in microporous AlPO catalysts, which share the $M(III)PO_4$ stoichiometry of de-lithiated LFP. The simultaneous presence of V^{4+} in Fe and P sites in LFP has been found to lead to a stable disproportionation into V^{3+}/Fe^{3+} and V^{5+}/P^{5+}, *i.e.* the two species observed by EXAFS, thus justifying the formation of V^{5+} on thermodynamic grounds.

ICP-AES was used to determine the vanadium content in the materials. The samples found to contain almost identical vanadium:iron ratios as expected from the precursor ratios (**Table 3**). The elemental ratios observed for LFVP(2.5) were consistent with the occupation of V ions on Fe and P sites. However, the elemental ratios of more heavily vanadium-doped samples are most consistent with substitution primarily on the Fe site. This is because the P levels are consistently deficient across the range of samples whilst the V levels increase at the cost of lower Fe levels. Therefore, EXAFS analysis of these higher level V-doped materials in conjunction with neutron powder diffraction (which is more sensitive to Li and can better differentiate between Fe and V than XRD) will be required to confirm the occupancy of V in

different sites, and the relative benefits of substitution on the Fe or P site. Furthermore, lithium deficiency increased with increasing vanadium content, which may indicate the presence of Li vacancies or Fe-substitution on the Li site, which have been observed for highly vanadium-doped samples elsewhere [16]. Therefore, the generation of Li^+ vacancies from vanadium doping will also contribute to the increased performance of the doped samples.

3.2. Electrochemical Characterization

Cyclic voltammetry (CV) tests were conducted for all heat-treated samples at a scan rate of 0.5 mV s^{-1}, and they confirmed the presence of the Fe^{2+}/Fe^{3+} couple at 3.45 V in all samples (**Figure 5a**). Additional electrochemical activity was observed in the first charge cycle of the sample ΔLFP2, and this activity was found to reduce between cycling (**Figure S10**). This activity can be attributed to the irreversible reaction of a minor amorphous ferric impurity present in the sample, and has been observed in other LFP samples [47]. Pure $LiFePO_4$ with the highest carbon loading (ΔLFP2) outperformed sample ΔLFP1, and hence ΔLFP1 is omitted hereafter for clarity (**Figure S11**). No additional activity due to vanadium was observed in the V-doped samples, even including ΔLFVP(10) and ΔLFVP(20), which contained an $LiV(P_2O_7)$ impurity. This is because the electrochemical activity of the $LiV(P_2O_7)$ phase is beyond the voltage window used in these tests [48]. A noticeable trend in peak current was observed between samples; the peak current increased with increasing vanadium doping up to 5 at%, but then decreased for higher V-dopant levels. This implied that the ΔLFVP(5) sample had the optimal electrochemical performance in the set of samples. The chemical diffusion coefficients of Li-ions within samples ΔLFP2, ΔLFVP(2.5) and ΔLFVP(5) were compared using the Randles-Sevcik equation (**Equation 1**), where I_p is the peak current (in Amperes), C is the initial concentration of Li-ions in the sample (mol cm^{-3}), A is the electrode area (cm^2), *D* is the diffusion coefficient (cm^2 s^{-1}), *n* is the number of

electrons involved in the Fe^{2+}/Fe^{3+} redox pair (and therefore $n = 1$), and v is the potential scan rate ($V\ s^{-1}$) [49].

$$I_p = (2.69 \times 10^5)\ C.A.D^{1/2}n^{3/2}v^{1/2}$$

Equation 1. The Randles-Sevcik equation.

Peak currents were obtained at potential scan rates of 0.05, 0.1, 0.2, 0.5, 1 and 2 $mV\ s^{-1}$ and plotted against $v^{1/2}$ (**Figure 5b**). The slopes obtained correspond to diffusion coefficients of 1.0×10^{-10}, 1.6×10^{-10} and 2.1×10^{-10} $cm^2\ s^{-1}$ for ΔLFP2, ΔLFVP(2.5) and ΔLFVP(5) respectively. These results should be regarded as qualitative and suggest that the 5 at% V-doped sample was expected to be the best performing at high discharge rates, and indicate enhanced Li^+ diffusion kinetics with doping. The voltage profiles of the samples also confirm the presence of the Fe^{2+}/Fe^{3+} couple (**Figure 5c**), and show no additional activity due to vanadium in any sample.

Despite the lower carbon content in the electrodes of the V-doped samples, they generally exhibited significantly better rate capability in constant-current tests compared the pure sample. While ΔLFVP(2.5) performed best at low current rates, the optimal high C-rate performance was observed for ΔLFVP(5) (**Figure 5d**), which is in agreement with other reports in the literature [8,11]. It is suggested that ΔLFVP(2.5) displayed the best low-rate performance as it had the smallest concentration of electrochemically inactive dopant and greatest Li^+ content. However, the capacity of ΔLFVP(5) and ΔLFVP(10) was greater at high discharge rates due to the greater concentration of Li^+ vacancies. This contrasting effect of dopants at low and high discharge rates has been observed previously by other researchers [50,51]. Increasing the dopant beyond 5 at% was detrimental to rate performance, and suggested that the presence of impurity phases had a negative effect, which has also been observed for this material previously [11]. Most importantly, further testing of this

composition gave an extremely high capacity of 119 mA h g^{-1} at a charge/discharge rate of 1500 mA h g^{-1} (*ca*. 9 C), which is impressive given the comparatively low 4 V voltage limit for the charge step (**Figure 5e**), and confirms the synergistic effect of core/shell carbon coating and vanadium doping. After testing at 9 C, the capacity at a slow charge/discharge rate (0.3 C) recovered to over 150 mA h g^{-1}, and confirmed the stability of the electrode at high C-rates. Long-term cycle stability tests (1000 cycles at 1 C) of ΔLFVP(5) showed excellent capacity retention of >96% over 200 cycles and >70% over 1000 cycles (**Figure S12**), thereby indicating these materials could be stable for high power applications.

4. Conclusions

We have synthesized a high performance carbon-coated core/shell vanadium-doped $LiFePO_4$ cathode *via* a continuous hydrothermal pilot-scale process. The combination of carbon-coating, nano-sizing and vanadium-doping dramatically improved the rate capability of the cathode material, with $LiFe_{0.95}V_{0.05}PO_4$ achieving a reversible specific discharge capacity of 119 mA h g^{-1} at a high discharge rate of 1500 mA g^{-1} (approximately 9 C). This was comparable to the best performances achieved in the academic literature for similar materials [10,15,52]. Moreover, when it is considered that these samples were optimized and made on a pilot-plant production scale of 6 kg per day, the result is even more remarkable and holds promise for future scale-up of larger cells in the future. The data from our combination of experimental and computational techniques are consistent with the assertion that vanadium doping can occur on both Fe and P sites within the structure. These types of doping have been observed separately, but never in conjunction previously. Furthermore, the crystal structure, crystallite size, impurity phase concentration and concentration of Li^+ vacancies varied consistently with increasing vanadium content, where the composition $LiFe_{0.95}V_{0.05}PO_4$ achieved the optimal balance of these factors. Further studies using EXAFS and neutron diffraction will provide more clarity on the precise site of V doping.

Acknowledgements

The EPSRC are thanked for funding the ELEVATE project (EP/M009394/1) and the Centre for Doctoral Training in Molecular Modelling & Materials Science (UCL, U.K.) which supports a studentship for Ian Johnson. Prof. John McArthur, Clement Denis, Joe Nolan and Marco Bersani are thanked for technical support, and Prof. Andy Dent and Dr. Stephen Parry at Diamond Light Source for their support on the B18 beamline. The simulations made use of the UCL Legion High Performance Computing Facility and the ARCHER supercomputer through membership of the UK's HPC Materials Chemistry Consortium (EPSRC grant EP/L000202).

References

[1] A.K. Padhi, K.S. Nanjundaswamy, J.B. Goodenough, J. Electrochem. Soc, 144 (1997) 1188-1194.
[2] J. Jiang, J.R. Dahn, Electrochem. commun., 6 (2004) 39-43.
[3] W.F. Howard, R.M. Spotnitz, J. Power Sources, 165 (2007) 887-891.
[4] O.K. Park, Y. Cho, S. Lee, H.-C. Yoo, H.-K. Song, J. Cho, Energy Environ. Sci., 4 (2011) 1621-1633.
[5] M. Park, X. Zhang, M. Chung, G.B. Less, A.M. Sastry, J. Power Sources, 195 (2010) 7904-7929.
[6] M. Gaberscek, R. Dominko, J. Jamnik, Electrochem. commun., 9 (2007) 2778-2783.
[7] S.-Y. Chung, J.T. Bloking, Y.-M. Chiang, Nat. Mater., 1 (2002) 123-128.
[8] J. Hong, C.S. Wang, X. Chen, S. Upreti, M.S. Whittingham, Electrochem. Solid-State. Lett., 12 (2009) A33-A38.
[9] N. Ravet, Y. Chouinard, J. Magnan, S. Besner, M. Gauthier, M. Armand, J. Power Sources, 97-98 (2001) 503-507.
[10] Y. Wang, Y. Wang, E. Hosono, K. Wang, H. Zhou, Angew. Chem. Int. Ed. Engl., 47 (2008) 7461-7465.
[11] M.-S. Chen, S.-H. Wu, W.K. Pang, J. Power Sources, 241 (2013) 690-695.
[12] H. Lin, Y. Wen, C. Zhang, L. Zhang, Y. Huang, B. Shan, R. Chen, Solid State Commun., 152 (2012) 999-1003.
[13] C. Sun, Z. Zhou, Z. Xu, D. Wang, J. Wei, X. Bian, J. Yan, J. Power Sources, 193 (2009) 841-845.
[14] M.-R. Yang, W.-H. Ke, J. Electrochem. Soc, 155 (2008) 729-732.
[15] F. Omenya, N. Chernova, S. Upreti, P.Y. Zavalij, K.-W. Nam, X.-Q. Yang, M. Whittingham, Chem. Mater., 23 (2011) 4733-4740.
[16] K. Harrison, C. Bridges, M. Paranthaman, C. Segre, J. Katsoudas, V. Maroni, J. Idrobo, J. Goodenough, A. Manthiram, Chem. Mater., 25 (2013) 768-781.
[17] F. Omenya, N.A. Chernova, Q. Wang, R. Zhang, M.S. Whittingham, Chem. Mater., 25 (2013) 2691-2699.
[18] J. Ma, B. Li, F. Kang, J. Phys. Chem. Solids, 73 (2012) 1463-1468.
[19] J. Ma, B. Li, H. Du, C. Xu, F. Kang, J. Electrochem. Soc, 158 (2011) 26-32.
[20] M. Islam, D. Driscoll, C. Fisher, P. Slater, Chem. Mater., 17 (2005) 5085-5092.
[21] J. Barker, M.Y. Saidi, J.L. Swoyer, Electrochem. Solid-State. Lett., 6 (2003) A53-A55.
[22] S. Yang, P.Y. Zavalij, M. Whittingham, Electrochem. commun., 3 (2001) 505-508.
[23] J. Chen, M. Whittingham, Electrochem. commun., 8 (2006) 855-858.

[24] S. Yang, X. Zhou, J. Zhang, Z. Liu, J. Mater. Chem, 20 (2010) 8086-8091.
[25] G. Meligrana, C. Gerbaldi, A. Tuel, S. Bodoardo, N. Penazzi, J. Power Sources, 160 (2006) 516-522.
[26] Y. Hakuta, K. Seino, H. Ura, T. Adschiri, H. Takizawa, K. Arai, J. Mater. Chem, 9 (1999) 2671-2674.
[27] T. Adschiri, Y.-W. Lee, M. Goto, S. Takami, Green Chem., 13 (2011) 1380-1390.
[28] Y. Hakuta, S. Onai, H. Terayama, J. Mater. Sci. Res., 17 (1998) 1211-1213.
[29] T. Adschiri, K. Kanazawa, K. Arai, J. Am. Ceram. Soc., 75 (1992) 1019-1022.
[30] C. Xu, J. Lee, A.S. Teja, J. Supercrit. Fluids, 44 (2008) 92-97.
[31] S.-A. Hong, S.J. Kim, K.Y. Chung, Y.-W. Lee, J. Kim, B.-I. Sang, Chem. Eng. J., 229 (2013) 313-323.
[32] A. Aimable, D. Aymes, F. Bernard, F. Le Cras, Solid State Ionics, 180 (2009) 861-866.
[33] K.H. Song, Y. Han, H.S. Nam, E.Y. Bang, S.J. Oh, I.J. Baek, S.Y. Kim, K.S. Han (Hanwha Corporation), US20120021288 A1, 2012.
[34] R. Gruar, C. Tighe, J. Darr, Ind. Eng. Chem. Res., 52 (2013) 5270-5281.
[35] W. Wagner, A. Pruß, J. Phys. Chem. Ref. Data, 31 (2002) 387-535.
[36] L. Lutterotti, S. Matthies, H.-R. Wenk, MAUD (Material Analysis Using Diffraction): a user friendly Java program for Rietveld Texture Analysis and more, in: Twelfth International Conference on Textures of Materials (ICOTOM-12), NRC Research Press, McGill University, Montreal, Canada, 1999, pp. 1599.
[37] B. Ravel, M. Newville, J. Synchrotron Radiat., 12 (2005) 537-541.
[38] N. Binstead, EXCURV98: CCLRC Daresbury Laboratory Computer Program, 1998
[39] X. Weng, J.K. Cockcroft, G. Hyett, M. Vickers, P. Boldrin, C.C. Tang, S.P. Thompson, J.E. Parker, J.C. Knowles, I. Rehman, I. Parkin, J.R.G. Evans, J.A. Darr, J. Comb. Chem., 11 (2009) 829-834.
[40] R. Quesada-Cabrera, X. Weng, G. Hyett, R.J.H. Clark, H.Z. Wang, J.A. Darr, ACS Comb. Sci., 15 (2013) 458-463.
[41] S. Kellici, K. Gong, T. Lin, S. Brown, R.J.H. Clark, M. Vickers, J.K. Cockcroft, V. Middelkoop, P. Barnes, J.M. Perkins, C.J. Tighe, J.A. Darr, Philos. Trans. A Math. Phys. Eng. Sci., 368 (2010) 4331-4349.
[42] S. Maurelli, G. Berlier, M. Chiesa, F. Musso, F. Corà, J. Phys. Chem. C, 118 (2014) 19879-19888.
[43] L. Gomez-Hortiguela, F. Corà, C.R.A. Catlow, Phys. Chem. Chem. Phys., 15 (2013) 6870-6874.
[44] P. Pelekanaki, F. Corà, C.R.A. Catlow, J. Am. Chem. Soc. (2014), submitted
[45] M.S. Islam, C.A.J. Fisher, Chem. Soc. Rev., 43 (2014) 185-204.
[46] X. Liu, Y. Zhang, S. Yi, C. Huang, J. Liao, H. Li, D. Xiao, H. Tao, J. Supercrit. Fluids, 56 (2011) 194-200.
[47] M. Cuisinier, J.-F. Martin, N. Dupre, R. Kanno, D. Guyomard, J. Mater. Chem, 21 (2011) 18575-18583.
[48] Y. Uebou, S. Okada, M. Egashira, J.-I. Yamaki, Solid State Ionics, 148 (2002) 323-328.
[49] N. Tanaka, R. Tamamushi, Electrochim. Acta, 9 (1964) 963-989.
[50] F. Omenya, N.A. Chernova, Q. Wang, R. Zhang, M.S. Whittingham, Chem. Mater., 25 (2013) 2691-2699.
[51] N. Meethong, Y.-H. Kao, W.C. Carter, Y.-M. Chiang, Chem. Mater., 22 (2010) 1088-1097.
[52] W.-J. Zhang, J. Electrochem. Soc, 157 (2010) 1040-1046.

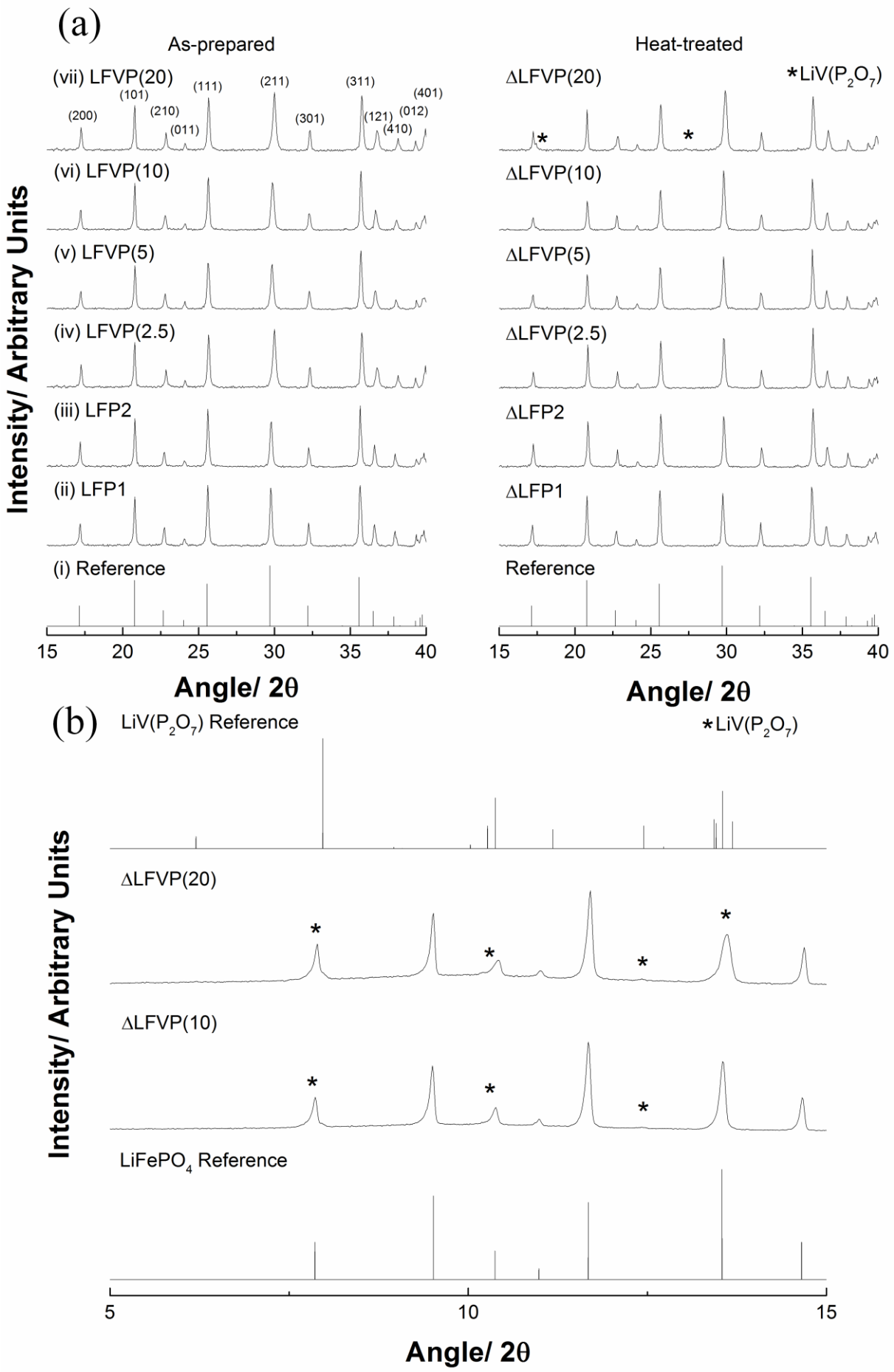
(a)
As-prepared
Heat-treated
(vii) LFVP(20)
(200)
(101)
(210)
(011)
(111)
(211)
(301)
(311)
(121)
(410)
(012)
(401)
ΔLFVP(20)
*LiV(P2O7)
(vi) LFVP(10)
ΔLFVP(10)
(v) LFVP(5)
ΔLFVP(5)
(iv) LFVP(2.5)
ΔLFVP(2.5)
(iii) LFP2
ΔLFP2
(ii) LFP1
ΔLFP1
(i) Reference
Reference
Intensity/ Arbitrary Units
15
20
25
30
35
40
Angle/ 2θ
(b)
LiV(P2O7) Reference
*LiV(P2O7)
ΔLFVP(20)
ΔLFVP(10)
LiFePO4 Reference
Intensity/ Arbitrary Units
5
10
15
Angle/ 2θ

Figure 1. (a) The XRD patterns (Cu-Kα radiation) of (i) a suitable reference pattern for olivine LFP (JCPDS card No: 00-040-1499), and (ii-vii) the as-prepared and heat-treated samples in the range 15 – 40° 2θ. (b) High-quality XRD (Mo-Kα radiation) patterns of ΔLFVP(10) and ΔLFVP(20) with $LiV(P_2O_7)$ (JCPDS card No: 00-085-2381) and $LiFePO_4$ (JCPDS card No: 00-040-1499) reference patterns in the range 5 – 15° 2θ.

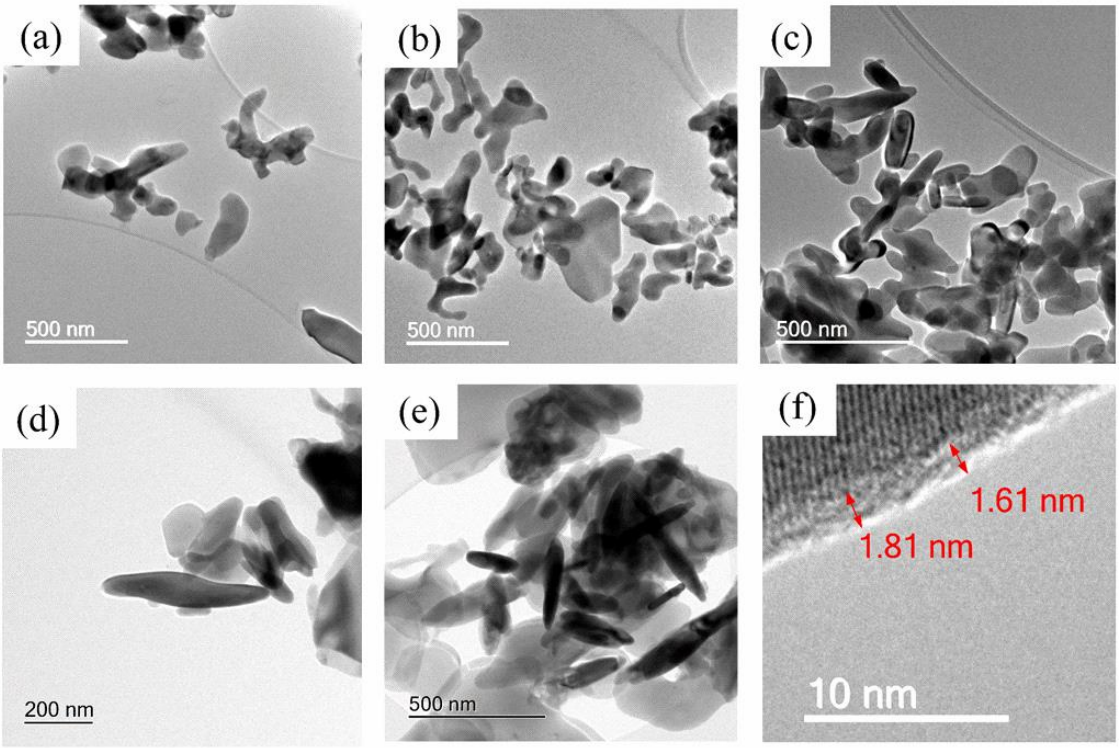

Figure 2. TEM images of (a) ΔLFP2, (b) ΔLFVP(2.5), (c) ΔLFVP(5), (d) ΔLFVP(10), (e) ΔLFVP(20), (f) the continuous carbon coating on ΔLFVP(20) made *via* CHFS and then heat-treated at 700 °C for 3 hours in argon.

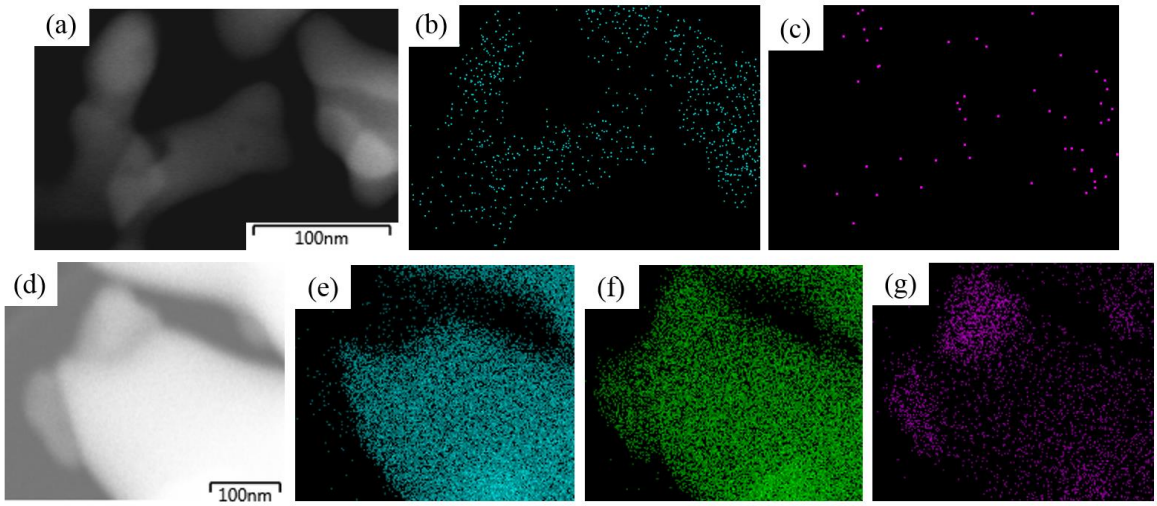

Figure 3. The EDS analysis of sample ΔLFVP(5), with (a) the darkfield image, (b) the Fe-Kα signals and (c) the V-Kα signals, and similar analysis of ΔLFVP(10) with (d) the darkfield image, (e) the Fe-Kα signals, (f) the P-Kα signals and (g) the V-Kα signals. The nucleation of a V-rich phase on the particle surface is evident from the elemental mapping. The contrast of image (c) was enhanced in ImageJ software.

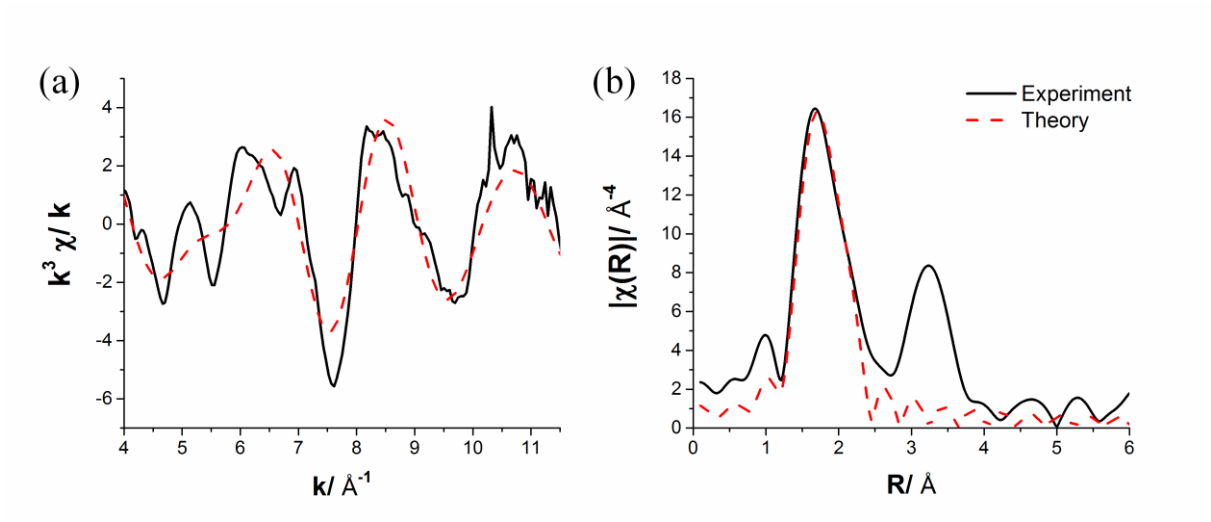

Figure 4. (a) EXAFS and (b) Fourier Transform of ΔLFVP(2.5) at the vanadium K-edge (*ca.* 5465 eV), where only the first coordination shell was fitted to obtain V-O bond lengths.

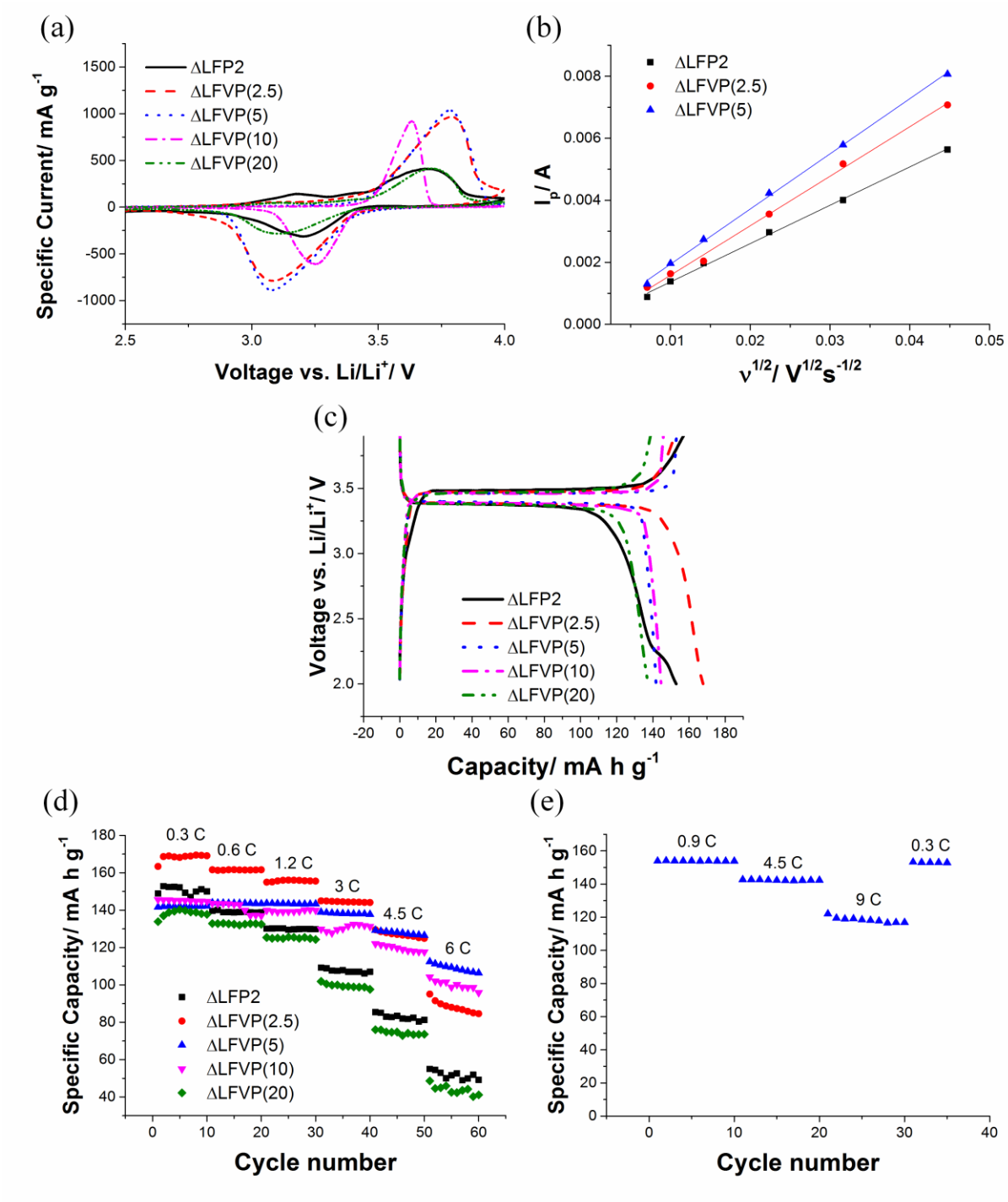

Figure 5. a) Cyclic Voltammetry tests (first cycle) at a scan-rate of 0.5 mV s^{-1}, b) Linear fits of peak current against $v^{1/2}$ for samples ΔLFP2, ΔLFVP(2.5) and ΔLFVP(5), c) Voltage vs. capacity plots of all samples (10th cycle at 0.3 C), d) Constant current tests at the C-rates shown and e) Further constant current tests of ΔLFVP(5) at the C-rates shown. The sample ΔLFVP(5) was consistently shown to be best performing across these tests.

Table 1. The lattice parameters of heat-treated samples from LeBail analysis.

Sample	*a* [Å][a]	*b* [Å][a]	*c* [Å][a]	*V* [Å][a]	R_{wp}
ΔLFP1	10.3231(2)	6.0033(1)	4.69394(9)	290.89(2)	7.62
ΔLFVP(2.5)	10.3235(2)	6.0040(1)	4.6960(1)	291.07(2)	7.62
ΔLFVP(5)	10.3208(2)	6.0019(1)	4.69692(9)	290.95(2)	7.85
ΔLFVP(10)	10.3241(2)	6.0014(1)	4.69782(8)	291.07(2)	7.72
ΔLFVP(20)	10.3022(3)	5.9762(1)	4.6997(1)	289.35(2)	8.44

[a] (Lattice parameters and their standard deviations are shown for the heat-treated samples)

Table 2. Calculated equilibrium V-O bond distances for different oxidation states, modes of incorporation and concentrations of V ions in LFP.

Oxidation state of V	Site	Conc. [%]	Supercell Formula	V-O bond length [Å]						**<V-O> [Å]**
2+	Fe	12.5	$Li_8Fe_7VP_8O_{32}$	2.1273	2.1273	2.1339	2.1770	2.1854	2.2050	**2.1593**
		12.5	$Li_1Fe_7VP_8O_{32}$	2.0608	2.0641	2.1771	2.1776	2.2107	2.2355	**2.1543**
		100	$Li_4V_4P_4O_{16}$	2.1271	2.1376	2.1376	2.1644	2.1876	2.1876	**2.1570**
3+	Fe	12.5	$Fe_7VP_8O_{32}$	1.933	1.953	2.088	2.0939	2.1127	2.128	**2.0514**
	(a)	12.5	$Mn_7VP_8O_{32}$	1.9379	1.9423	2.0568	2.0708	2.1220	2.1261	**2.0426**
		100	$V_4P_4O_{16}$	1.9277	1.9681	2.0876	2.0876	2.1042	2.1042	**2.0467**
4+	Fe (b)	12.5	$Li_1Fe_6VP_8O_{32}$	1.8270	1.8584	1.8874	1.9653	2.0921	2.0955	**1.9542**
	(c)	12.5	$Li_1Fe_6VP_8O_{32}$	1.8253	1.8509	1.8911	1.9668	2.0898	2.1074	**1.9552**
5+	P	12.5	$Fe_8P_7VO_{32}$	1.6636	1.6868	1.7356	1.7381			**1.7060**
		6.25	$Fe_{16}P_{15}VO_{64}$	1.6649	1.6859	1.7336	1.7356			**1.7045**
		12.5	$Li_8Fe_8P_7VO_{32}$	1.6872	1.7013	1.7169	1.7245			**1.7075**
		100	$Fe_4V_4O_{14}$	1.6642	1.6917	1.7450	1.7450			**1.7115**
		100	$Li_4Fe_4V_4O_{16}$	1.6954	1.6968	1.7285	1.7285			**1.7123**

[a] (V in $LiMnPO_4$ for comparison) [b] (Li in Fe site) [c] (Interstitial Li and Fe vacancy)

Table 3. The composition of the vanadium-doped samples found by ICP-AES.

Sample	Li/P[a]	Fe/P[a]	V/P[a]	P/P[a]
LFP1	1.05	1.04	0.00	1.00
LFVP(2.5)	1.01	1.00	0.03	1.00
LFVP(5)	0.97	0.96	0.05	1.00
LFVP(10)	1.01	0.94	0.09	1.00
LFVP(20)	0.92	0.85	0.19	1.00

[a] (The concentrations were normalized to phosphorous in these samples)